

Dual-band Fourier domain optical coherence tomography with depth-related compensations

Miao Zhang,¹ Lixin Ma,² and Ping Yu^{1,*}

¹Department of Physics and Astronomy, University of Missouri, Columbia, Missouri 65211, USA

²Department of Radiology, University of Missouri and Harry S. Truman Memorial Veteran's Hospital, Columbia, Missouri 65211, USA
yuping@missouri.edu

Abstract: Dual-band Fourier domain optical coherence tomography (FD-OCT) provides depth-resolved spectroscopic imaging that enhances tissue contrast and reduces image speckle. However, previous dual-band FD-OCT systems could not correctly give the tissue spectroscopic contrast due to depth-related discrepancy in the imaging method and attenuation in biological tissue samples. We designed a new dual-band full-range FD-OCT imaging system and developed an algorithm to compensate depth-related fall-off and light attenuation. In our imaging system, the images from two wavelength bands were intrinsically overlapped and their intensities were balanced. The processing time of dual-band OCT image reconstruction and depth-related compensations were minimized by using multiple threads that execute in parallel. Using the newly developed system, we studied tissue phantoms and human cancer xenografts and muscle tissues dissected from severely compromised immune deficient mice. Improved spectroscopic contrast and sensitivity were achieved, benefiting from the depth-related compensations.

©2013 Optical Society of America

OCIS codes: (110.4500) Optical coherence tomography; (170.3880) Medical and biological imaging.

References and links

1. D. Huang, E. A. Swanson, C. P. Lin, J. S. Schuman, W. G. Stinson, W. Chang, M. R. Hee, T. Flotte, K. Gregory, C. A. Puliafito, and et, "Optical coherence tomography," *Science* **254**(5035), 1178–1181 (1991).
2. C. Hitzenberger, E. Goetzinger, M. Sticker, M. Pircher, and A. Fercher, "Measurement and imaging of birefringence and optic axis orientation by phase resolved polarization sensitive optical coherence tomography," *Opt. Express* **9**(13), 780–790 (2001).
3. K. W. Gossage, T. S. Tkaczyk, J. J. Rodriguez, and J. K. Barton, "Texture analysis of optical coherence tomography images: feasibility for tissue classification," *J. Biomed. Opt.* **8**(3), 570–575 (2003).
4. P. Cimalla, J. Walther, M. Mehner, M. Cuevas, and E. Koch, "Simultaneous dual-band optical coherence tomography in the spectral domain for high resolution *in vivo* imaging," *Opt. Express* **17**(22), 19486–19500 (2009).
5. S. Kray, F. Spöler, M. Först, and H. Kurz, "High-resolution simultaneous dual-band spectral domain optical coherence tomography," *Opt. Lett.* **34**(13), 1970–1972 (2009).
6. X. Zhang, J. Hu, R. W. Knighton, X.-R. Huang, C. A. Puliafito, and S. Jiao, "Dual-band spectral-domain optical coherence tomography for *in vivo* imaging the spectral contrasts of the retinal nerve fiber layer," *Opt. Express* **19**(20), 19653–19659 (2011).
7. M. Choma, M. Sarunic, C. Yang, and J. Izatt, "Sensitivity advantage of swept source and Fourier domain optical coherence tomography," *Opt. Express* **11**(18), 2183–2189 (2003).
8. J. F. de Boer, B. Cense, B. H. Park, M. C. Pierce, G. J. Tearney, and B. E. Bouma, "Improved signal-to-noise ratio in spectral-domain compared with time-domain optical coherence tomography," *Opt. Lett.* **28**(21), 2067–2069 (2003).
9. M. Pircher, E. Gotzinger, R. Leitgeb, A. F. Fercher, and C. K. Hitzenberger, "Speckle reduction in optical coherence tomography by frequency compounding," *J. Biomed. Opt.* **8**(3), 565–569 (2003).
10. S. Kray, M. Lenz, F. Spöler, and H. Kurz, "Increased tissue contrast by high resolution simultaneous dual-band optical coherence tomography in three dimensions," in Proceedings of SPIE-OSA Biomedical Optics (Optical Society of America, 2011), 809209.
11. Z. Hu, Y. Pan, and A. M. Rollins, "Analytical model of spectrometer-based two-beam spectral interferometry," *Appl. Opt.* **46**(35), 8499–8505 (2007).

12. Acquiring from GigE Vision Cameras with Vision Acquisition Software”, retrieved <http://www.ni.com/white-paper/5651/en>.
13. G. Lamouche, C. E. Bisaillon, S. Vergnole, and J. P. Monchalin, “On the speckle size in optical coherence tomography,” in *Proc. SPIE 6847, Coherence Domain Optical Methods and Optical Coherence Tomography in Biomedicine XII*, 2008), 684724–684726.
14. H. Lin and P. Yu, “Speckle mechanism in holographic optical imaging,” *Opt. Express* **15**(25), 16322–16327 (2007).
15. Y. Zhang, X. Li, L. Wei, K. Wang, Z. Ding, and G. Shi, “Time-domain interpolation for Fourier-domain optical coherence tomography,” *Opt. Lett.* **34**(12), 1849–1851 (2009).
16. C. Dorrer, N. Belabas, J.-P. Likforman, and M. Joffre, “Spectral resolution and sampling issues in Fourier-transform spectral interferometry,” *J. Opt. Soc. Am. B* **17**(10), 1795–1802 (2000).
17. R. Leitgeb, W. Drexler, A. Unterhuber, B. Hermann, T. Bajraszewski, T. Le, A. Stingl, and A. Fercher, “Ultrahigh resolution Fourier domain optical coherence tomography,” *Opt. Express* **12**(10), 2156–2165 (2004).
18. Y. Yasuno, S. Makita, T. Endo, G. Aoki, M. Itoh, and T. Yatagai, “Simultaneous B-M-mode scanning method for real-time full-range Fourier domain optical coherence tomography,” *Appl. Opt.* **45**(8), 1861–1865 (2006).
19. B. Baumann, M. Pircher, E. Götzinger, and C. K. Hitzenberger, “Full range complex spectral domain optical coherence tomography without additional phase shifters,” *Opt. Express* **15**(20), 13375–13387 (2007).
20. M. Zhang, P. Yu, and L. Ma, “Removal of Mirror Image Using Reference Beam Phase Modulation in Dual-Band Fourier-Domain Optical Coherence Tomography,” in OSA Technical Digest (online) (Optical Society of America, 2012), JTh3J.5.
21. S. Makita, T. Fabritius, and Y. Yasuno, “Full-range, high-speed, high-resolution 1 microm spectral-domain optical coherence tomography using BM-scan for volumetric imaging of the human posterior eye,” *Opt. Express* **16**(12), 8406–8420 (2008).
22. R. K. Wang, “Fourier domain optical coherence tomography achieves full range complex imaging in vivo by introducing a carrier frequency during scanning,” *Phys. Med. Biol.* **52**(19), 5897–5907 (2007).
23. A. Ozcan, A. Bilenca, A. E. Desjardins, B. E. Bouma, and G. J. Tearney, “Speckle reduction in optical coherence tomography images using digital filtering,” *J. Opt. Soc. Am. A* **24**(7), 1901–1910 (2007).
24. K. K. H. Chan and S. Tang, “High-speed spectral domain optical coherence tomography using non-uniform fast Fourier transform,” *Biomed. Opt. Express* **1**(5), 1309–1319 (2010).
25. W. F. Cheong, S. A. Prahl, and A. J. Welch, “A review of the optical properties of biological tissues,” *IEEE J. Quantum Electronics* **26**(12), 2166–2185 (1990).
26. J. M. Schmitt, A. Knüttel, M. Yadlowsky, and M. A. Eckhaus, “Optical-coherence tomography of a dense tissue: statistics of attenuation and backscattering,” *Phys. Med. Biol.* **39**(10), 1705–1720 (1994).
27. A. Hojjatoleslami and M. R. N. Avanaki, “OCT skin image enhancement through attenuation compensation,” *Appl. Opt.* **51**(21), 4927–4935 (2012).
28. M. J. A. Girard, N. G. Strouthidis, C. R. Ethier, and J. M. Mari, “Shadow Removal and Contrast Enhancement in Optical Coherence Tomography Images of the Human Optic Nerve Head,” *Invest. Ophthalmol. Vis. Sci.* **52**(10), 7738–7748 (2011).
29. M. R. Arnfield, J. Tulip, and M. S. McPhee, “Optical propagation in tissue with anisotropic scattering,” *IEEE Trans. Biomed. Eng.* **35**(5), 372–381 (1988).
30. S. G. Adie, B. W. Graf, A. Ahmad, P. S. Carney, and S. A. Boppart, “Computational adaptive optics for broadband optical interferometric tomography of biological tissue,” *Proc. Natl. Acad. Sci. U.S.A.* **109**(19), 7175–7180 (2012).
31. V.-F. Duma, K. S. Lee, P. Meemon, and J. P. Rolland, “Experimental investigations of the scanning functions of galvanometer-based scanners with applications in OCT,” *Appl. Opt.* **50**(29), 5735–5749 (2011).
32. K. Zhang and J. U. Kang, “Graphics processing unit accelerated non-uniform fast Fourier transform for ultrahigh-speed, real-time Fourier-domain OCT,” *Opt. Express* **18**(22), 23472–23487 (2010).
33. X. Li, G. Shi, and Y. Zhang, “High-speed optical coherence tomography signal processing on GPU,” *J. Phys. Conf. Ser.* **277**, 012019 (2011).
34. Y. Watanabe, “Real time processing of Fourier domain optical coherence tomography with fixed-pattern noise removal by partial median subtraction using a graphics processing unit,” *J. Biomed. Opt.* **17**(5), 050503 (2012).
35. Y. Wang, C. M. Oh, M. C. Oliveira, M. S. Islam, A. Ortega, and B. H. Park, “GPU accelerated real-time multi-functional spectral-domain optical coherence tomography system at 1300 nm,” *Opt. Express* **20**(14), 14797–14813 (2012).
36. L. Ma, P. Yu, B. Veerendra, T. L. Rold, L. Retzloff, A. Prasanphanich, G. Sieckman, T. J. Hoffman, W. A. Volkert, and C. J. Smith, “In vitro and in vivo evaluation of Alexa Fluor 680-bombesin[7-14]NH₂ peptide conjugate, a high-affinity fluorescent probe with high selectivity for the gastrin-releasing peptide receptor,” *Mol. Imaging* **6**(3), 171–180 (2007).
37. A. F. Prasanphanich, L. Retzloff, S. R. Lane, P. K. Nanda, G. L. Sieckman, T. L. Rold, L. Ma, S. D. Figueroa, S. V. Sublett, T. J. Hoffman, and C. J. Smith, “In vitro and in vivo analysis of [(64)Cu-NO₂A-8-Aoc-BBN(7-14)NH₂]: a site-directed radiopharmaceutical for positron-emission tomography imaging of T-47D human breast cancer tumors,” *Nucl. Med. Biol.* **36**(2), 171–181 (2009).
38. F. J. van der Meer, D. J. Faber, M. C. Aalders, A. A. Poot, I. Vermes, and T. G. van Leeuwen, “Apoptosis- and necrosis-induced changes in light attenuation measured by optical coherence tomography,” *Lasers Med. Sci.* **25**(2), 259–267 (2010).
39. X. Li, J. C. Ranasinghesagara, and G. Yao, “Polarization-sensitive reflectance imaging in skeletal muscle,” *Opt. Express* **16**(13), 9927–9935 (2008).

40. H. He, N. Zeng, R. Liao, T. Yun, W. Li, Y. He, and H. Ma, "Application of sphere-cylinder scattering model to skeletal muscle," *Opt. Express* **18**(14), 15104–15112 (2010).
41. Y. Mao, S. Chang, E. Murdock, and C. Flueraru, "Simultaneous dual-wavelength-band common-path swept-source optical coherence tomography with single polygon mirror scanner," *Opt. Lett.* **36**(11), 1990–1992 (2011).
42. R. Zhu, J. Xu, C. Zhang, A. C. Chan, Q. Li, P. Chui, E. Y. Lam, and K. K. Wong, "Dual-Band Time-Multiplexing Swept-Source Optical Coherence Tomography Based on Optical Parametric Amplification," *IEEE J. Sel. Top. Quantum Electron.* **18**(4), 1287–1292 (2012).
43. R. Weissleder and M. J. Pittet, "Imaging in the era of molecular oncology," *Nature* **452**(7187), 580–589 (2008).
44. Q.-Y. Cai, P. Yu, C. Besch-Williford, C. J. Smith, G. L. Sieckman, T. J. Hoffman, and L. Ma, "Near-infrared fluorescence imaging of gastrin releasing peptide receptor targeting in prostate cancer lymph node metastases," *Prostate* **73**(8), 842–854 (2013).

1. Introduction

Optical coherence tomography (OCT) is a non-invasive imaging technique that provides high speed cross sectional images in biological tissues [1]. OCT acquires interferograms of sample and reference in a low coherence interferometer, and reconstructs the interferograms into intensity images to show sample microstructures. However, as commonly known in optical microscopy, it is difficult to differentiate tissue types merely based on the intensity images [2, 3]. Dual-band OCT, which uses light sources covering two distinct wavelength bands, has been shown to be a simple and powerful functional extension of intensity images in OCT [4–6]. Among various OCT techniques, dual-band Fourier domain OCT (FD-OCT) takes advantage of high speed and interferometric stability of spectral domain schematics, and shows a better signal-to-noise ratio than that of time domain OCT techniques [7, 8].

Dual-band FD-OCT gains general benefits of using two light sources in OCT. For example, the intensity images from two wavelength bands are averaged as a frequency compound image for speckle reduction [9], and the two intensity images are subtracted as a differential image that provides spectroscopic information. The frequency compound image and the differential image can be encoded in a single color image, straightforwardly showing both the de-speckled intensity and spectroscopic information. A color schematic using a Hue Saturation Value (HSV) color map has been proven to be successful in spectroscopic display and tissue contrast [10]. In the HSV color map, the intensity difference mainly affects the brightness while the spectroscopic information is displayed as color contrast. However, when using a color map for the spectroscopic information, a false spectroscopic contrast exists due to the signal attenuation below the sample surface, which is a result of scattering and absorption along the depth of the sample [4]. In addition, the depth-related fall-off [11] in FD-OCT also exacerbates a spectroscopic deviation. These problems generally exist in the dual-band FD-OCT and are independent of color schematics. Accordingly, previous dual-band FD-OCT imaging systems could not correctly give the tissue spectroscopic information. To solve these problems, both hardware and software should be modified in the dual-band FD-OCT imaging system.

In this work, we designed a new dual-band full-range FD-OCT system, and incorporated a depth-related compensation algorithm to correct spectroscopic data. To validate the new algorithm, we studied tissue phantoms and human PC-3 prostate cancer xenograft tumor and muscle tissues dissected from severely compromised immune deficient (SCID) mice.

2. System description

There are three requirements for the depth-related compensations (see section 4 for detailed explanation): (1) an intensity balance from two wavelength bands, (2) an overlap of two wavelength images, and (3) a high speed program for image acquisition and process. The FD-OCT setup, shown in Fig. 1, consists of a source unit, a probe unit, and a detection unit. A single mode fiber and a fiber polarization controller (FPC030, Thorlabs, Inc.) connect the source unit and the probe unit. The source unit includes two superluminescent light emission diodes (SLEDs) in distinct bands of 820 nm and 760 nm with bandwidths of 20 nm (SLD-370-HP2-TOW2, Superlum and EXS7505-B001, Exalos). The beam profiles of the broadband lights are shaped into round using mounted anamorphic prism pairs (GPA-3X-8.0, CVI Melles Griot). The two broadband lights are combined by a dichroic mirror.

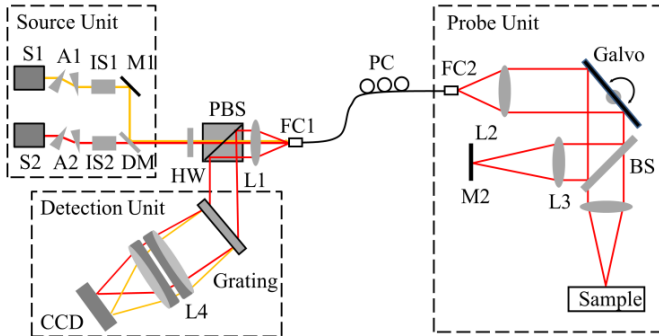


Fig. 1. Experimental setup of dual-band full range FD-OCT system. S1-S2: superluminescent light emission diodes. A1-A2: anamorphic prism pairs. IS1 and IS2: optical isolators. M1-M2: mirrors. DM: dichroic mirror. HW: half-wave plate. PBS: polarization beam splitter. FC1-FC2: FC/APC fiber collimators. L1-L3: achromatic lenses. L4: achromatic lenses pair. PC: polarization controller. Galvo: galvanometer scanner. BS: 30/70 beam splitter.

The intensities between the two SLED lights are balanced using a broadband half-wave plate (AHWP05M-980, Thorlabs Inc.) and a polarization beam splitter (PBS) (PBS202, Thorlabs Inc.). The single mode fiber delivers the lights from the source unit to the probe unit, and sends the recombined interferometric signals back to the PBS. A galvanometer (galvo) scanner (6210H, Cambridge Technology) is used in the probe unit, providing a two-dimensional scan. The numerical aperture (N.A.) of objective lens (L3 in Fig. 1) is 0.015 providing the depth of focus of 8 mm. The power on the sample is 200 μ W. In addition to the intensity balance, the benefit of this design is that more broadband light sources can be added into the imaging system without any major modification.

The detection unit consists of a holographic transmission grating (1200 grooves/mm, Wasatch Photonic), a high speed line-scan charge coupled device (CCD) camera (12-bit, 1024 pixels, 56 kHz, ruL1024-57gm, GigE interface, Basler Runner), and a pair of achromatic lenses. Since the spectra from the two wavelength bands are acquired in the same single line scan CCD camera, two reconstructed FD-OCT images are intrinsically overlapped.

The data acquisition and image process of dual-band images are accelerated by using multi-threads and parallel computing. The GigE interfaced CCD camera is connected to an Intel PRO/1000 network card and is controlled by a National Instrument (NI) high performance driver. With this interface, the data transfer bandwidth reaches as high as 125 Mbytes/s [12] that meets the demand for the CCD camera running in its full speed. The synchronized trigger signal for the CCD acquisition and the triangular wave for the galvo scan are generated by a NI PXI 6521 DAQ card. A LabVIEW program is developed for the system (Fig. 2). To achieve a real time data acquisition, process and display, the program runs four basic threads in parallel: (1) the data acquisition thread, (2) the image processing thread, (3) the image display and storage thread, and (4) the galvo and CCD control thread. The connections between the threads are fulfilled by the data queues, such that thread 1 & 2 and thread 2 & 3 become two pairs of producer-and-consumer loops. A main benefit the producer/consumer pattern brings is that the producer does not need to wait for the consumer. For instance, thread 1 can continue the next data acquisition while thread 2 is still processing the current data. In other words, all threads execute in parallel. Further, since the trigger signal is hardware-generated from the high-speed DAQ and the CCD works in a continuously triggered mode, the imaging speed is not limited by the electronics.

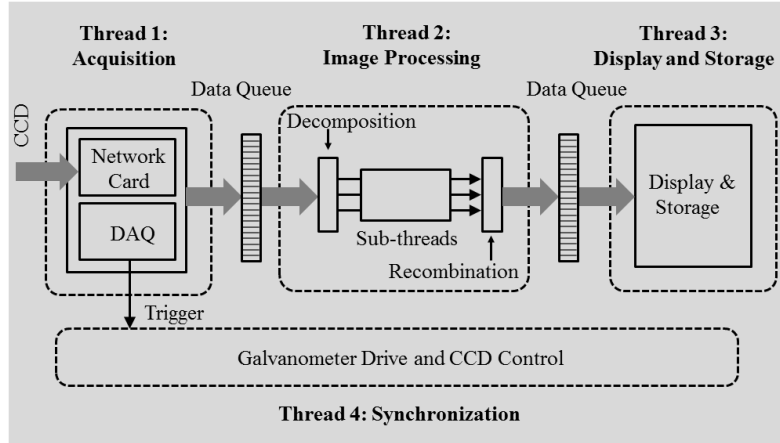


Fig. 2. Structure of LabVIEW program for acquiring, processing and displaying dual-band FD-OCT data. Thread 1 & 2 and thread 2 & 3 are two producer-and-consumer loops that are connected by data queues. Thread 1, 2, 3 and 4 execute in parallel, and the image processing thread is further decomposed into 3 sub-threads.

3. System characterization and data process

We used a Cartesian coordinate system to describe the 3D imaging mode: z is the depth/axial direction; x is the fast scanning direction (lateral); y is the slow scanning direction. So A-scans are along the z axis, B-scans are in the x-z plane, and C-scans are in the x-y plane.

For each wavelength band, 512 pixels in the CCD are used to acquire the 50 nm width spectrum (40 nm effective). The spectral resolution is 0.1 nm and the resulting full-range depth limit is 2.4 mm in tissue (suppose a refractive index of 1.4). Limited by the signal beam diameter on the sample and the spectral bandwidths of the SLEDs, the lateral and depth resolutions of the FD-OCT system are calculated to be 30 μm and 11 μm , respectively, and measured to be 31 μm and 15 μm (in tissue). The speckle size is a useful parameter for determining the spatial interval between neighboring A-scans in the mirror image suppression and for selecting the filter size in image smoothing [13]. Experimental results of the speckle size are shown in Fig. 3 (see reference [14] for the algorithm to determine the speckle size using normalized self-covariance functions).

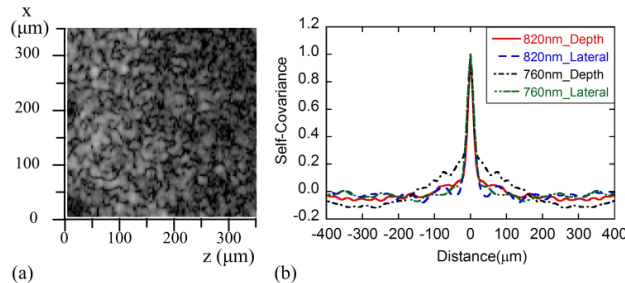


Fig. 3. (a) A speckle pattern in a B-scan FD-OCT image. (b) Normalized self-covariance functions of speckle patterns. A Gaussian fitting shows that the lateral and depth speckle sizes (FWHM) are 19 μm and 21 μm for 820 nm, and 28 μm and 23 μm for 760 nm, respectively.

Spectral interferometric data are subtracted by a background before further data process. Then an interpolation from wavelength-space to wavenumber-space is performed. We use the time-domain interpolation approach [15] that is based on the zero padding method [16, 17]. It decreases the depth-related fall-off while significantly reduces the interpolation time. The interpolated signals are separated into two data sets according to the two wavelength bands.

The wavenumber intervals of each image are fixed, so that no image resizing is necessary. Figure 4 gives the depth dependent sensitivity measurement using an aluminum reflector with an uneven surface (it gives a broad sample frequency bandwidth, which is similar to real sample in the case of phase modulation for mirror image suppression). The intensity fall-off along the depth is shown in Fig. 4(a). The fall-off is 8 dB along a 1 mm axial depth. Figure 4(b) gives the result after the fall-off correction. A perfect position matching of two data sets is observed in Fig. 4.

FD-OCT suffers from the mirror image artifact that comes from the inverse Fourier transform of real-value spectral interferograms. To suppress the mirror image artifact, phase-shifting techniques are often used [18, 19]. In our setup, the phase shift is introduced by x axis scan of the galvo and the tilted reference mirror [20]. Spatial interval between A-lines is selected according to the speckle size determined in Fig. 3, i.e. the sample ratio (the ratio of speckle size and A-line interval) is four. A cosine tapered window in the time domain [21, 22] is used for filtering the mirror image. Finally, a 3×3 adaptive wiener filter [23] is used for de-speckling and smoothing the data before the reconstruction of a spectroscopic image. This filter size is smaller than the ratio of the speckle size ($\sim 30 \mu\text{m}$) to the pixel size ($\sim 5 \mu\text{m}$) in the FD-OCT image, so that the smoothing won't decrease the effective resolution.

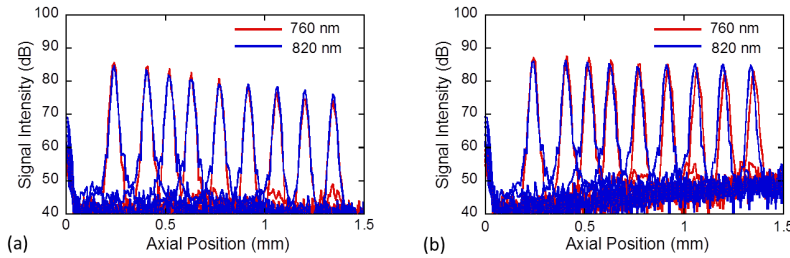


Fig. 4. Intensity fall-off and compensation along the z axis. Data are acquired using an aluminum reflector placed at different depth positions. (a) Before the depth-related fall-off compensation. (d) After the depth-related fall-off compensation.

As commonly used in dual-band OCT, a differential image is defined as an image obtained by subtracting the 820 nm image from the 760 nm image, while a frequency compound image is an average of the two images. The final spectroscopic image is displayed in HSV schematics, representing an overlay of the differential image on the frequency compound image. The Hue value (H) ranges from 0 to 250, corresponding to -10 dB to 10 dB in the differential image map. Therefore the red color represents a stronger intensity in the longer wavelength while the blue color means a stronger intensity in the shorter wavelength. If the spectroscopic image color is green, intensities for the two wavelengths are identical. The Value (V) changes from 0 to 1, mapping from 0 to 15 dB in the frequency compound image. The Saturation value (S) is set to be 0.8.

Using an AMD Phenom II X6 CPU, we achieved a processing speed of 16 k A-lines per second with mirror suppression (512 pixel/A-scan), which is comparable to that of non-uniform fast Fourier transform method (90 k without mirror suppression) [24]. Approximately, it takes 100 ms for a two-band 450×800 intensity image process and an additional 80 ms for a HSV image reconstruction.

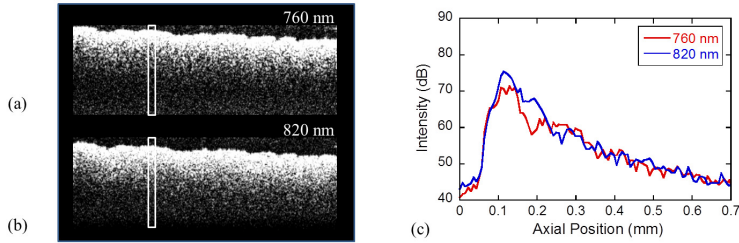


Fig. 5. FD-OCT Images (B-scans) of an infrared viewing card. (a) Image of 760 nm. (b) Image of 820 nm. (c) Depth intensity graph showing an average of 50 A-lines.

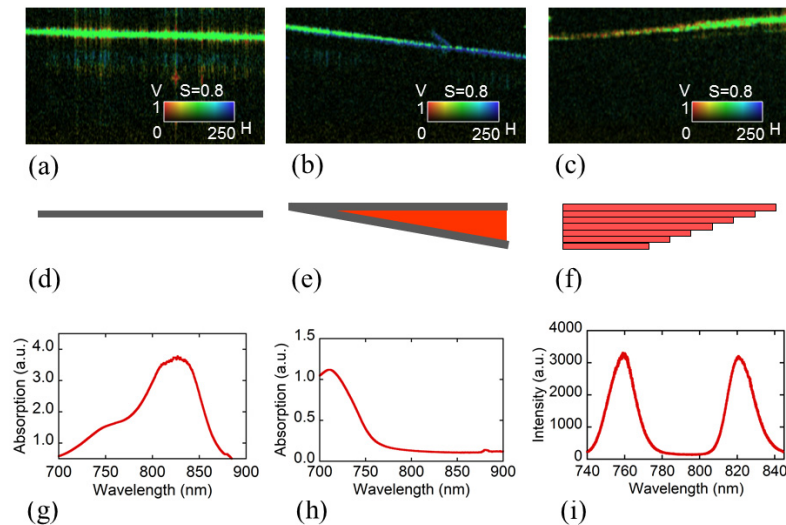


Fig. 6. (a) Dual-band FD-OCT images (B-scan) of a reflector. (b) A reflector behind a wedge-shaped sample with stronger absorption in 820 nm. (c) A reflector behind a stacking sample with stronger absorption in 760 nm. (d) Schematic diagram of the reflector. (e) Schematic diagram of the wedge sample. (f) Schematic diagram of the stacking sample. (g) Absorption spectrum of near infrared dye in the wedge sample of (e). (h) Absorption spectrum of the color filter in the stacking sample of (f). (i) The spectrum of two SLEDs. Inserts in (q), (b), and (c) are the HSV color map ($S = 0.8$, V changes from 0 to 1, and H ranges between 0 and 250).

The signal-to-noise ratio (SNR) of the imaging system is calibrated using an infrared viewing card that provides depth-related scattering signals. Figure 5 shows a typical calibration result in which the SNRs of the two wavelengths are equal along the penetration depth. After the calibration, the dual-band FD-OCT image of a reflector shows a uniform green color (Fig. 6(a) and 6(d)). To qualitatively illustrate the color map of the dual-band FD-OCT system, two wedge-shaped samples with strong absorption bands at 820 nm or 760 nm are designed. The first sample is a home-made glass triangular cuvette (Fig. 6(e)) filled with a methanol solution of near infrared dye (ADS832WS, absorption peak at 832 nm, American Dye Source, Inc.). Figure 6(g) gives the spectrum of this dye. The second sample is made by stacking several pieces of brilliant blue plastic color filter (#69, Roscolux) in a step fashion (Fig. 6(f)). The absorption peak of the color filter is at 710 nm, as shown in Fig. 6(h). These samples are placed in front of a reflector for dual-band FD-OCT imaging. The color of resulted image changes from green to blue in Fig. 6(b) and from red to green in Fig. 6(c) since the thickness of the absorption materials is different along the x (lateral) direction in the samples. Figure 6(i) is the spectrum for two SLEDs. The color bars in the insert of Fig. (a), (b), and (c) are used for all color images in this paper.

4. Depth-related fall-off and attenuation compensations

4.1 Model

As shown in Fig. 4, the FD-OCT signal has a depth-related fall-off that is determined by the spectral resolution of the spectrometer. Since the grating and focal lens have a limited dispersion ability and the line scan CCD camera has a finite pixel size and separation, the detection sensitivity decreases exponentially as the path length difference between the signal and reference increases [11]. Another factor is that the spot sizes for the rays close to the edge of the lens are larger than those at the center due to the aberrations. In addition, the focal plane may be curved rather than flat [11]. Those factors are significant in our dual-band FD-OCT because the spectrometer needs to sample two separate wavelength bands. Another problem, which is named as depth-related attenuation, is generally present in OCT. Light signals reflected from deeper parts of the tissue sample are attenuated by the scattering and absorption of the tissue [25], and the light also loses spatial coherence progressively as it penetrates deeper into the tissue [26].

When interpreting the intensity image generated by a single band OCT, researchers used to tolerate the aforementioned fall-off and attenuation, while having to keep in mind the presence of the intensity degradation along the depth. However, images whose intensity directly reflects the reflectivity are still preferred. As early as in 1994, Schmitt et al. sketched a depth-related attenuation compensation for samples with uniform attenuation coefficient based on the Beer-Lambert law [26]. But the compensations for general samples are complicated. It is until recently that Ali et al. brought the compensation method to multi-layered skin imaging [27]. Girard et al. applied the compensation to optic nerve head imaging, using an algorithm borrowed from ultrasound imaging [28].

For dual-band FD-OCT, the requirement for the compensation is more imperative, considering that not only intensity but also spectroscopic information are encoded in the HSV images. The depth-related fall-off and attenuation will decrease the V, hence darken the color. H will also be changed if the signal intensity of one wavelength is decreased down to the noise level, or the signals of two wavelength bands are different at a specific location inside the sample, such that they experience different attenuation. The change of H will totally change the displayed color. As can be seen from the simulation results in the next section, both changes will give false spectroscopic information. To solve these problems in a dual-band FD-OCT, we developed a compensation algorithm for image post processing.

The principle of depth-related fall-off compensation is relatively intuitive. As mentioned before, the depth-related fall-off can be measured using a reflector placed at different depth positions. In the image processing step, the premeasured fall-off is simply added to the original image.

For the compensation of depth-related attenuation, we developed an algorithm based on the method used by Ali and Girard. Typically, scattering is two orders stronger than absorption in tissue in the near IR range [25]. So in our case, scattering is assumed to be dominant. Furthermore, since the forward scattering and back scattering are often stronger than the scattering at other angles [29], it is straightforward to suppose that the attenuation is proportional to the intensity of backscattered light along the path in the sample. We define the compensation value of a given pixel to be proportional to the sum of the compensated pixels' values in front of it. The compensation of each pixel can be calculated starting from the pixel e according to

$$I_{\text{compensated}}(n) = I(n) \cdot (1 + \alpha \sum_{i=e}^{n-1} I_{\text{compensated}}(i)), \quad (1)$$

where $I(n)$ is the original value of the pixel number n and $I_{\text{compensated}}(n)$ is the value after the compensation. These values are represented in dB scale. α is the constant coefficient. Equation (1) works for both falling slope and rising slope of the intensity profile along the

path. If there is a strong scatter in the path (corresponding to a rising slope), the pixels in the deep tissue get a larger compensation. The initial condition is given by

$$I_{\text{compensated}}(e) = I(e). \quad (2)$$

This means that there is no attenuation on the tissue surface. The pixel number e refers to the top edge position of the tissue. In the case of uniform sample where the attenuation coefficient is a constant, this equation is identical to the Beer-Lambert law.

It needs to be mentioned that in our algorithm, the lateral resolution is assumed to be invariant along the depth since a low N.A. objective lens is used. For high N.A. cases, a correction beforehand will be needed [30].

To apply this algorithm to the dual-band FD-OCT system, the first step is to find out the top edge of the tissue sample. More specifically, the frequency compound image is filtered by an 11×11 adaptive wiener filter (based on our experiment, this size gives the most precise edge tracking result), and then the edge pixel e is determined by finding the increased slope position. As the top edge position could be any value in the field of view, the overlap between two wavelength images is critical for a successful compensation.

4.2 Simulation

To further elaborate the effect of depth-related fall-off and attenuation on dual-band FD-OCT imaging and evaluate our compensation algorithm, a simulation is performed using several pairs of 2D arrays representing raw images of a reflector with desired reflecting properties.

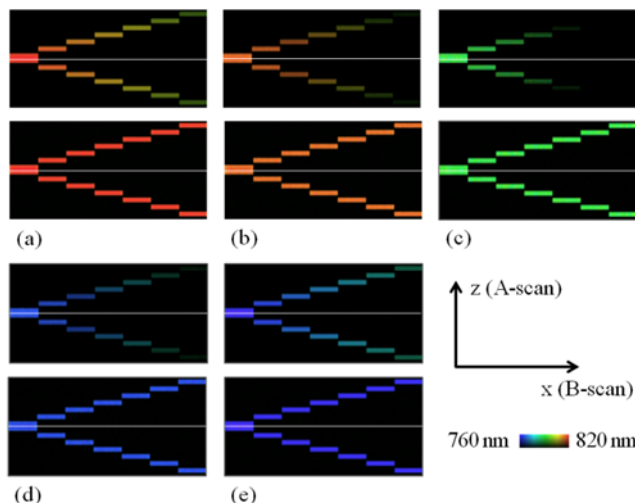


Fig. 7. Simulation results of the depth-related fall-off and compensation. The white lines indicate the zero-cross. The upper images from (a) to (e) are the simulation results before the compensation. Undesired color change when moving away from the zero-cross is clearly seen. The lower images show uniform color after the compensation. From (a) to (e), the reflectivity of longer wavelength decreases while the reflectivity of shorter wavelength increases. The signal intensity for the reflector at the zero-cross: (a) 45 dB at 760 nm, 60 dB at 820 nm. (b) 48.25 dB at 760 nm, 56.75 dB at 820 nm. (c) 51.5 dB at 760 nm, 51.5 dB at 820 nm. (d) 56.75 dB at 760 nm, 48.25 dB at 820 nm. (e) 65 dB at 760 nm, 45 dB at 820 nm.

Because the depth-related fall-off starts from the zero-cross, the simulated data arrays represent images of the reflector at different steps moving away from the zero-cross. The following conditions apply here: (1) The reflectivity of the reflector decreases at a rate of 8 dB/mm for each wavelength starting from the zero-cross, which is a simulation of depth-related fall-off. (2) From Fig. 7(a) to 7(e), the reflectivity at 760 nm increases while the reflectivity at 820 nm decreases. In addition, a noise of 40 dB is added in each image. The results simulate samples with different reflectivity at two wavelength bands. As we pointed

out in 4.1, the undesired color change is clearly shown in the upper row images in Fig. 7. Using the fall-off compensation algorithm, the image colors are recovered as clearly shown in the lower row images in Fig. 7.

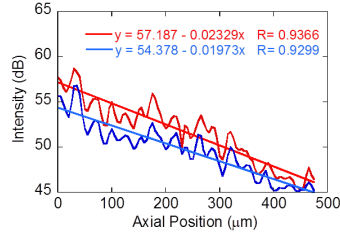


Fig. 8. Typical A-lines and linear fitting from a FD-OCT image of the tumor sample. Two lines correspond to different illuminate intensities between the two wavelength bands.

To simulate attenuation compensation using Eqs. (1) and (2), two representative A-lines from a homogeneous tumor tissue are acquired and fitted, as shown in Fig. 8. These two A-lines are from different illuminating intensities between the two wavelength bands and their fitted parameters are used to compose simulated A-lines. For a homogeneous sample with different scattering coefficients in the two interested wavelength bands, we expect a larger decreasing slope for larger scattering, and vice versa.

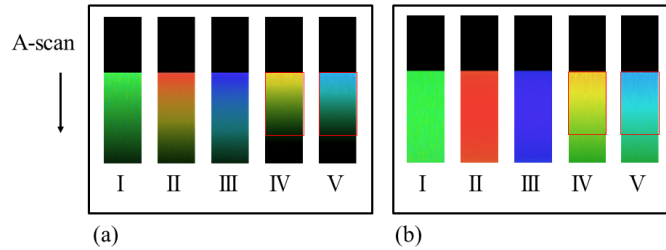


Fig. 9. Simulation results of depth-related attenuation and compensation. (a) shows images after depth-related fall-off compensation but without attenuation compensation, while (b) shows images after both compensations. Color uniformity is significantly improved in (b). In the simulation, $\alpha = 1.8 \times 10^{-5}$. Red rectangles indicate the effective regions in the A-lines. Below these regions, original signals are below noise, the compensated results are noisy and meaningless. Five color bars I to V correspond to expanded A-lines from samples with different backscattering properties (see section 4.2 for detail description).

The simulation results in Fig. 9 are shown in five color bars corresponding to expanded A-lines from samples with different backscattering properties. The noise is 40 dB. Figure 9(a) shows the results without the compensation while Fig. 9(b) shows the results after the compensation. These five bars can be classified into three cases. First, we consider a simple case when the backscattered signals are not wavelength dependent. In this case, we expect a constant green color in the reconstructed HSV image that contains the correct spectroscopic information. However, as can be seen in the bar I of Fig. 9(a), even after the depth-related fall-off compensation, the apparent darker color is still observed. Second, we treat an extreme case for a sample with a large wavelength-dependent scattering. In this case, the detected signal for one wavelength is at the noise level. We expect that the image shows a constant red (Fig. 9(a) II) or blue (Fig. 9(a) III). Third, we use two sets of fitted parameters in Fig. 8 to simulate a sample that has a “normal” wavelength dependent scattering (Fig. 9(a) IV and V). Since these two A-lines are taken at the same position, we expect an improved color contrast in the red rectangular of the reconstructed image. Figure 9(a) IV and V shows the color change beyond the red rectangular region due to the noise.

Although the five simulation cases have different parameters, all final compensated results show an improvement in the color uniformity, i.e. the spectroscopic information is corrected and consistent, as shown in Fig. 9(b). It needs to be pointed out that the different illuminate

intensity gives different colors, as shown in Fig. 9 IV and V. Therefore, the intensity balance is important to correctly provide spectroscopic information in the dual-band FD-OCT system. In these simulations, α is determined to be 1.8×10^{-5} for both wavelengths based on the compensation effect to uniform tissue sample. This α value is large enough to compensate the attenuation in deep tissue, but still small enough to prevent overcompensation. For other samples, the α value can be determined a similar method.

In these simulations, speckle caused fluctuation is not taken into consideration. However, our algorithm is dependent only on the total effects on the route, so it is speckle resistant. This can be seen in Fig. 10 and 11 in next section.

4.3 Examples of tissue phantom and muscle tissue for both compensations

The compensation algorithm was tested using a tissue phantom (1 mm cuvette filled with 1- μm diameter polystyrene microspheres in distilled water). Figure 10 shows A-lines and images before and after applying the compensations. The peak at 650 μm is from the front surface of the cuvette, while the peak at 1700 μm is a reflection from the back surface. The back surface serves as a reflector. After the compensations, the image of the back surface has a uniform color. In HSV scheme, the V value of the back surface peak is 0.3 before the compensations and 0.7 after the compensations.

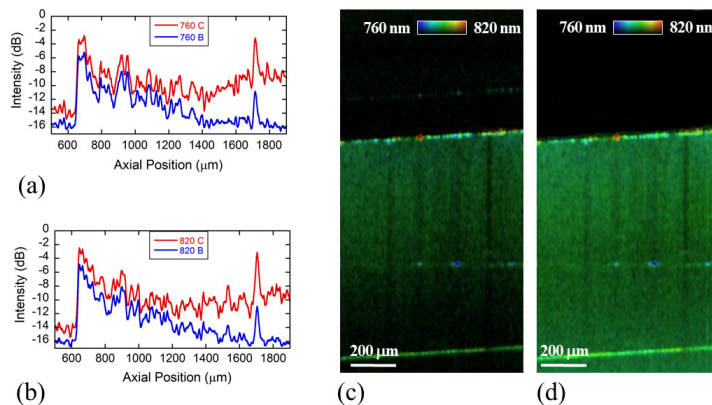


Fig. 10. Tissue phantom results. A-lines before (blue) and after (red) the compensations of the tissue phantom at (a) 760 nm and (b) 820 nm. Images of the tissue phantom before (c) and after (d) the compensations.

Figure 11 shows a step-by-step process of the two compensations on a mouse muscle tissue. The time interval of sequential A-scans is 200 μs and the exposure time is set to be 195 μs . Since each frame contains 800 A-scans and the galvo works at an 80% duty-cycle triangular waveform scan mode, the frame rate for the acquisition is 5 Hz. The galvo has a high stability in such condition [31]. The acquired 450 \times 800 pixels images are then resized and clipped to 420 \times 700 pixels, corresponding to 2.1 mm (z) \times 3.5 mm (x) in real space.

The original dual-band FD-OCT image is shown in Fig. 11(a). From Fig. 11(a) to 11(b), the depth-related fall-off compensation is applied, showing a significant color restoration in the top region of the muscle sample. In Fig. 11(c), the top edge of the sample is precisely located and marked as a red line. In Fig. 11(d), the attenuation compensation is applied based on Fig. 11(b) and 11(c). It is clear that the color contrast in deeper region is improved. Finally in Fig. 11(e), the noise is removed since the top edge is found in Fig. 11(c).

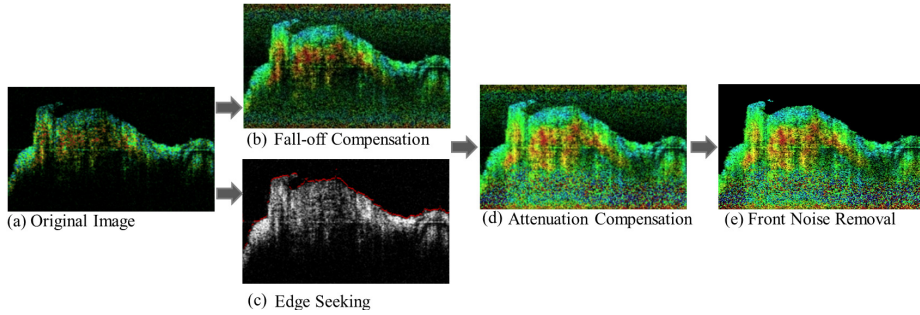


Fig. 11. Dual band FD-OCT images of muscle tissue. (a) Original image. (b) Image with fall-off compensation. (c) Image shows that the sample edge is found. The intensity image is a frequency compound image. (d) Image with fall-off and attenuation compensations. It can be seen that the color information is improved in the final image. The levitated noise is discussed in section 5. It can be removed by edge seeking, as shown in (e).

4.4 Evaluation of results

In Fig. 12, the compensation results for two sets of A-lines (A-line #1 and A-line #2) from the muscle tissue are shown. The A-lines in Fig. 12(a) and 12(b) are from a sample region where the signals of two wavelengths are similar, i.e. green region in the HSV image. The A-lines in Fig. 12(c) and 12(d) are from a sample region with higher signal intensity in longer wavelength band, i.e. red region in the HSV image. It is clear that the attenuation induced signal degradations in deep, effective regions (axial position 1200–1400 μm in (a) and (b), 800–1000 μm in (c) and (d)) are compensated, while the signal peaks are still maintained. In other words, the sensitivity and contrast in deep region are both improved.

As a quantitative evaluation, we calculated and showed the contrast-to-noise ratio (CNR) in Fig. 13, corresponding to the four cases in Fig. 12. The CNR is defined as

$$CNR = \frac{(\mu_r - \mu_b)}{\sqrt{\sigma_r^2 + \sigma_b^2}}. \quad (3)$$

where μ_b and σ_b stand for the mean and variance in the background noise regions (700 – 800 μm in A-line #1, 100 – 200 μm in A-line #2), respectively. μ_r and σ_r represent the mean and variance in the region of interest (1200–1400 μm in A-line #1 and 800–1000 μm in A-line #2), respectively. Similar results were shown in a reference paper [27].

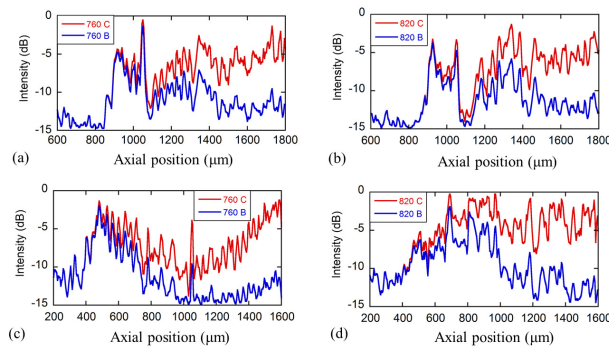


Fig. 12. Depth-related fall-off and attenuation compensations of A-lines. Blue: original; Red: after the compensation. (a) and (b): A-line #1 from a tissue showing similar signals at the two wavelengths. (c) and (d): A-line #2 from a tissue showing different signals at the two wavelengths. Both tissues showed improved contrast after the compensations in deep, effective region (axial position 1200–1400 μm in (a) and (b), 800–1000 μm in (c) and (d)).

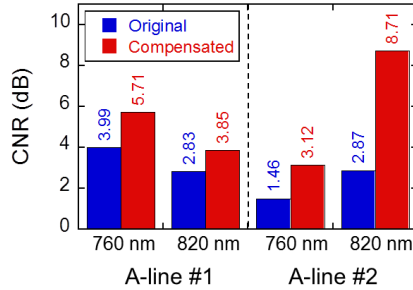


Fig. 13. Quantitative evaluation of the compensated A-lines in Fig. 12. Four pairs of CNR for original A-lines (blue) and compensated A-lines (red) correspond to Fig. 12(a), 12(b), 12(c) and 12(d), respectively.

4.5. Speed issue for compensations

The compensation algorithm is applied independently on different A-lines, so it is easy to run in different parallel threads. The total computation time of a frame is about 250 ms on a PC with AMD Phenom II X6 CPU. Without parallel processing, it would take more than 1000 ms. Graphic processing unit (GPU) computing in fast OCT data analysis [32–35] will be our future development to further speed up the proposed compensation process.

5. Imaging results

To evaluate the newly developed dual-band FD-OCT system and depth-related compensation algorithm, we studied tumor tissues and muscle tissues. The human PC-3 prostate cancer tumors were grown on the flanks of severely compromised immune deficient (SCID) mice for four weeks; the tumors (about 10 mm in diameter) and muscle tissues were then harvested and immediately fixed in 4% formalin solution (Fisher Scientific) [36]. The animal experiments were conducted in accordance with the highest standards of care as outlined in the National Institute of Health guidelines for Care and Use of Laboratory Animals and the Policy and Procedures for Animal Research at the Harry S. Truman Memorial Veterans' Hospital.

Figure 14 shows dual-band FD-OCT images of a PC-3 tumor xenograft. For a homogeneous tumor tissue, a spectroscopic OCT HSV image should give a uniform color. However, in the image before compensation (Fig. 14(a)), the region far away from the zero-cross and deep tissue show a different color, as a result of depth-related fall-off and attenuation corresponding to the simulations in Fig. 7 and Fig. 9, respectively. Figure 14(b) shows improved color uniformity after the depth-related compensations.

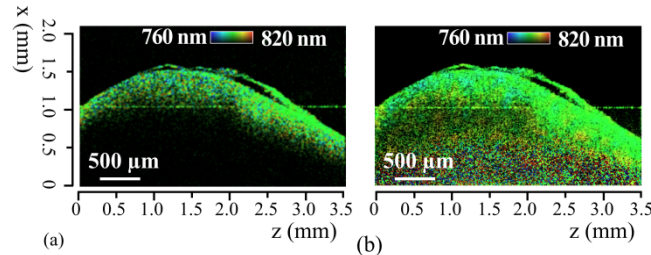


Fig. 14. Dual-band FD-OCT images of tumor tissue without (a) and with depth-related fall-off and attenuation compensations (b). The deeper regions where red and blue pixels are interlaced correspond to dark region in original image are due to the noise. These regions can easily be removed by setting a threshold. The image size is 420 × 700 pixels covering $2.1 \times 3.5 \text{ mm}^2$.

It needs to be noted that in Fig. 14(b) the interlaced red and blue pixels in the deeper region of the tumor tissue are due to the levitated noise after the compensations. These

regions can easily be removed by setting a threshold, but we keep them to maintain the image continuity. The horizontal line at the middle of the image is due to the autocorrelation artifact that commonly presents in FD-OCT.

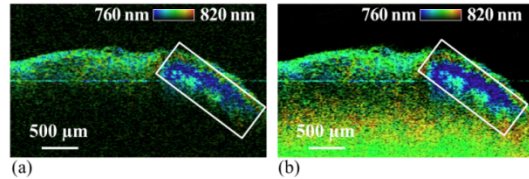


Fig. 15. Dual-band FD-OCT images of heterogeneous tumor tissue without (a) and with (b) depth-related compensations.

To further evaluate the dual-band FD-OCT system and the compensation algorithm, several heterogeneous PC-3 tumors with necrotic centers were examined. Figure 15 shows a heterogeneous spectroscopic color region from a necrotic center which was confirmed on magnetic resonance imaging (MRI) (see discussion). An interesting feature is that the blue color in the white rectangular box does not change before and after the compensations although the spectroscopic contrast is improved. Furthermore, we are interested in the color change in the homogeneous tumor tissues. To see the effect clearly, 3D image data were acquired with multiple frames scanning along the y-axis galvo mirror. The acquired 3D data are re-organized in Fig. 16 showing a C-scan in the x-y section. The image pixels of the tumor tissue in the x-y section reside in different depths inside the sample. Before the compensations, some image pixels in the red rectangular box have a blue color, showing a potential heterogeneous tissue similar to the blue color in the white rectangular box (Fig. 16 (a)). However, after the depth-related compensations, the blue color pixels in the red rectangular box are changed into green (Fig. 16(b)). The compensations also fill the darkened hole in the red rectangular box.

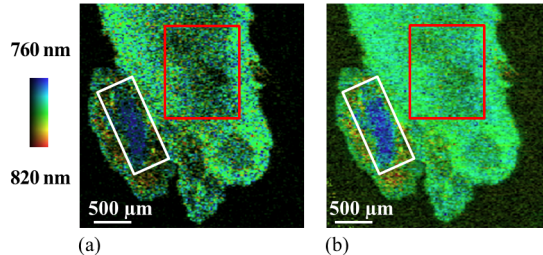


Fig. 16. Dual-band FD-OCT C-scan images in the x-y section for a heterogeneous tumor tissue without (a) and with (b) depth-related compensations.

Moreover, dual-band FD-OCT with the depth-related compensations was applied to image muscle tissues adjacent to the tumors from SCID mice. Figure 17(a) and 17(b) are original images which show a range of colors and structures. Figure 17(c) to 17(d) are the corresponding images after depth-related compensations. Improved sensitivity and spectroscopic contrast are observed in the compensated images of the muscle tissues. The results further demonstrate the effectiveness of the depth-related compensation algorithm for the images containing complex spectroscopic information.

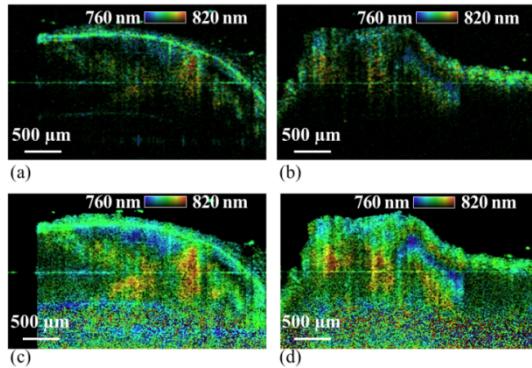


Fig. 17. Dual-band FD-OCT images of muscle tissues before ((a) and (b)) and after ((c) and (d)) the depth-related compensations. The colored regions reveal characteristic cellular morphology and arrangement in muscle, which is discussed in section 6.

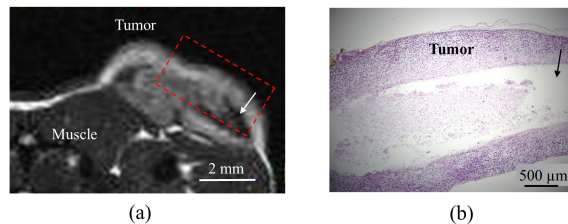


Fig. 18. (a) Diffusion weighted-MRI performed *in vivo* on a SCID mouse bearing human PC-3 tumor and (b) the corresponding hematoxylin and eosin stained histology graph ($5 \mu\text{m}$ section thickness) of the tumor in Fig. 15. The region in red rectangle corresponds to the imaging window in Fig. 15. Arrows indicate the necrotic tissue.

6. Discussion on image results

Efforts have been made to interpret the color contrast in the dual-band FD-OCT images. Because the signal intensities for two wavelengths are balanced, the color difference in the image reflects spectroscopic scattering and/or birefringence of the tissue samples. In our case, no strong absorbers within two wavelength bands exist in the tissues. The differences caused by possible absorption for two wavelength bands are negligible. Therefore, the color regions should be highly correlated to the sample structural characteristics.

The dual-band FD-OCT images of tumor and muscle tissues show a range of colors that the blue and red color represents the signals at short and long wavelength, respectively. The image of uniform tumor tissue with a green color corresponds to the same scattering for both wavelengths, as shown in Fig. 14. On the other hand, the tumor tissues in Fig. 15 and Fig. 16 appear in both blue and green color regions. To characterize the tumor tissues, we performed a microscopic histological image stained (Fig. 18(b)) where cancer cells were hematoxylin and eosin (H&E). We further compared the FD-OCT images with the diffusion weighted-MRI (DW-MRI) of the tumor (Fig. 18(a)) acquired on a 7 T MRI system (Varian Inc., CA). We found that the blue color regions in Fig. 15 and 16 correspond to tumor necrotic centers that were shown as low intensity signals on DW-MRI and H&E image [37]. In solid PC-3 prostate tumors, the cancer cells are densely packed and the cancer cells are relatively large ($\sim 10 \mu\text{m}$ in diameter) comparing to normal healthy cells, whereas the necrotic tissues are dead cancer cells and fluid-like tissues. In the necrotic tissue, the cell membrane defects, and the cells, even their organelles, lose integrity [38]. This specific morphology of necrotic cancer cells is responsible for the strong scattering signals at the short wavelength in Fig. 15 and 16.

In Fig. 17, the dual-band FD-OCT images of muscle tissues show abundant colors ranging from orange to red. In contrary to tumor cells, muscle cells are elongated and form muscle fibers that are arranged in parallel bundles. Considering this characteristic morphology, the strong color contrasts in the muscle tissues are due to the birefringence of muscle fibers. Recently, P. Cimalla et al studied human nail plates using dual-band OCT, and successfully explained that the observed periodic layered structures in the nail plates correlated with birefringence induced polarization state changes [4]. Experimental and theoretical studies have shown that the propagation of polarized light in muscle is modulated by strong birefringence, diattenuation, multiple scattering induced depolarization and the sarcomere diffraction effect [39, 40]. When placing a polarizer in front of the sample with different orientations, we found that the colors exchange in the dual-band FD-OCT images since the incident and collected light were at different polarization states. This phenomenon indicates that the birefringence of muscle fibers is responsible for the intensity difference between the two wavelengths in the muscle samples.

We show that after the depth-related compensations, the newly developed dual-band FD-OCT system provides an improved spectroscopic contrast and sensitivity. In practice, most dual-band FD-OCT modalities have a large wavelength difference between the two bands although some work used two light sources with small wavelength separation [41, 42]. If the intensity balance is maintained, our work can be extended to other dual-band FD-OCT since there is no wavelength limitation in the algorithm. The technique demonstrates an ability to distinguish solid tumor and necrotic tissues based on the wavelength-correlated signals. The result has a practical significance for clinical specialists such as radiation oncologists, especially in imaging-guided radiotherapy [43, 44] for cancer patients.

7. Conclusion

We have built a new full-range dual-band FD-OCT system with balanced and overlapped images from two wavelength bands at 760 nm and 820 nm, and developed an algorithm for compensating depth-related discrepancy and attenuation. Both simulations and experimental results showed an improved spectroscopic contrast and sensitivity in PC-3 prostate tumor tissues and muscle tissues. The new dual-band FD-OCT system with the depth-related compensation algorithm demonstrates an improvement in tissue differentiation.

Acknowledgments

This work was supported by the National Science Foundation Career Award BES-0746871 (PY) and Department of Defense Prostate Cancer Research Program W81XWH-09-2-0176 (LM). We acknowledge the supports from the Harry S. Truman VA Hospital.